Bulletin of the Seismological Society of America, Vol. 92, No. 8, pp. 3165–3179, December 2002

Borehole Response Studies at the Garner Valley Downhole Array, Southern California

by Luis Fabián Bonilla, Jamison H. Steidl, Jean-Christophe Gariel, and Ralph J. Archuleta

Abstract The Garner Valley Downhole Array (GVDA) consists of a set of seven downhole strong-motion instruments ranging from 0- to 500-m depth. One of the objectives of this experiment is to estimate site response and study wave propagation as the energy travels from the bedrock underneath the site up through the soil column. The GVDA velocity structure is studied by computing synthetic accelerograms for a small event located at an epicentral distance of 10 km. These synthetics simulate well the data recorded at the borehole stations. In addition, theoretical transfer functions are calculated using the obtained velocity model and compare well with the empirical transfer functions from 54 recorded events. It is also observed that the downgoing wave effect is predominant in the first 87 m and is strongly reduced at depth. Using the velocity structure at GVDA and the transfer function results, it has also been possible to develop a simple method to compute the incident wave field, which is needed in nonlinear site response for instance.

Recently there have been many comparative studies between horizontal-to-vertical (H/V) spectral ratios and traditional spectral ratios. Although many of these studies show that H/V spectral ratios can reproduce the shape of the site response curve, most show differences in the amplitude level. In the case of Garner Valley, where we have both surface and multiple borehole instruments, we find that this discrepancy in amplitude of the site response estimates is because the vertical component has significant site response associated with it due to *S*-to-*P* conversions that begin in the weathered granite boundary at 87-m depth.

Introduction

The near-surface geological site conditions in the upper tens of meters are one of the dominant factors in controlling the amplitude and variation of strong ground motion and the damage patterns that result from large earthquakes. Our understanding of these site effects comes primarily from surface recordings. In recent years, however, the increase in the number of borehole instruments provides a significant step forward in directly measuring the effects of surface geology. Borehole measurements provide critical constraints on our methods for interpreting surface observations. In addition, they have provided some of the most provocative results about basic seismological and earthquake engineering problems. For example, borehole measurements provided direct *in situ* evidence of nonlinearity (e.g., Seed and Idriss, 1970; Wen *et al.*, 1994; Zeghal and Elgamal, 1994; Iai *et al.*, 1995; Sato *et al.*, 1996; Aguirre and Irikura, 1997; Satoh *et al.*, 2001a); they have invited a reevaluation of the use of surface-rock recordings as input motion to soil columns (e.g. Satoh *et al.*, 1995; Steidl *et al.*, 1996; Boore and Joyner, 1997), and they have provided basic information about scaling properties of the spectra of earthquakes of different magnitudes (e.g., Kinoshita, 1992; Abercrombie, 1997).

Experimental studies of site effects need to consider simultaneously a reference hard-rock site and sites on alluvium. In most cases, two methods are used. In the first, rock and alluvium sites are located at the surface (e.g., Borcherdt, 1970; Hartzell, 1992; Margheriti *et al.*, 1994; Field and Jacob, 1995; Kato *et al.*, 1995; Field, 1996; Hartzell *et al.*, 1996; Su *et al.*, 1996; Bonilla *et al.*, 1997). However, two problems can be encountered. First, if the reference site is far from the studied sites, the incident wave field does not have the same characteristics for the different stations. Second, it has been shown (Steidl *et al.*, 1996) that a true reference site, that is, corresponding to a site located on high-velocity geological formations, is very difficult to find due to the ubiquitous presence of a weathered layer near the surface.

In the second method, the reference site is located at depth inside the rock formation. In this case, the incident wave field is assumed to be similar for all stations, but other problems related to the presence of the free surface have to be faced. At any depth, the particle motion contains the incident wave field and the reflections from the free surface as well as from the different velocity interfaces in the soil column. In the frequency domain, the destructive interference between the incident wave field and the downgoing waves may produce holes in the ground-motion spectrum (Steidl *et al.*, 1996). Consequently, a direct spectral ratio between the surface and the total motion at depth generally produces pseudoresonances where these holes are present. This phenomenon is known as the downgoing wave effect. This poses a problem when computing transfer functions in vertical arrays, because the direct spectral ratio may be affected by these waves. If no reflections are present in the ground motion, as in the case of free-surface records, they correspond to the incident wave field directly. In this study, the transfer function computed using the motion of the reference site as the incident wave field will be denoted as "outcrop response." Conversely, when the motion of the reference site is the total downhole wave field, the transfer function will be denoted as "borehole response."

In this article, we use the Garner Valley Downhole Array (GVDA) project to conduct a precise study of the borehole response in a specific well-studied site. First, the velocity and attenuation models of the GVDA site are fine tuned using time domain simulations, and the general characteristics of wave propagation at depth are studied. Second, using the standard spectral ratio technique, the transfer functions between different depths and surface and the effect of the downgoing wave field are discussed. Finally, the applicability of the horizontal-to-vertical (H/V) spectral ratio to estimate site response is evaluated by comparing its results with those obtained in the previous sections.

The Garner Valley Downhole Array Experiment

The GVDA experiment was designed to study site effects in a simple context, namely in the presence of simple flat layers overlaying a hard-rock formation. The *in situ* measurement of ground motion at different levels within the soil column and in the bedrock below provides a rich data set to examine the effects of attenuation, amplification, and nonlinear soil behavior as the wave field propagates up through the soil column (Archuleta *et al.*, 1992, 1993).

Geological Conditions

The GVDA test site is located in southern California at a latitude of 33°40.127′ N and a longitude of 116°40.427′ W in the North American Datum NAD 83 coordinate system (Fig. 1). The site is located in a narrow valley within the Peninsular Ranges Batholith. The near-surface structure consists of an ancestral lake bed with soft alluvium to a depth of 18–25 m over a layer of weathered granite, with the competent granitic bedrock interface at 87-m depth. The valley is about 4 km at its widest and 10 km long trending northwest–southeast, parallel to the major faults in southern California. The valley floor is at an elevation of 1310 m and the surrounding mountains reach maximum heights of just over 3000 m.

The upper 18–25 m consist of soil rich in organics and alluvium. Soil types present are silty sand, sand, clayey sand, and silty gravel. There is a gradual transition from alluvium to decomposed granite from 18 to 25 m. Decomposed granite consisting of gravely sand exists between 25 and 87 m. At 87 m the contact with hard competent bedrock is reached. The bedrock is granodiorite of the Southern California Peninsular Ranges batholith. The water table fluctuates at the GVDA site depending on the season and rainfall totals. In wetter years the water table is at or just below the surface in the winter and spring months. In the summer and fall months, or the entire dry years, the water table drops to 1 to 3 m below the surface.

Seismotectonic Background

Strike-slip and reverse faulting associated with the Pacific–North American plate boundary in the southern California region represent the major tectonic elements. Primarily, GVDA was required to be in a seismically active region that would provide both weak- and strong-motion data. Its location, 7 km from the main trace of the San Jacinto fault system and 35 km from the San Andreas fault helps to meet these criteria (Fig. 1). The San Jacinto fault system is historically the most active strike-slip fault system in southern California. The slip rate of 10 mm/y and the absence of a large earthquake since at least 1890 on a 40 km zone of the Anza segment leads to a relatively high probability for a magnitude 6.0 or larger event in the near future (Sharp, 1967; Rockwell *et al.*, 1990). The GVDA is located in an area where good local control on the location of earthquakes exists. The U.S. Geological Survey (USGS)/Caltech Southern California Seismic Network (SCSN) of high-gain velocity transducers and the University of California–San Diego 10-station array of velocity transducers in the Anza region provide excellent coverage of the local and regional seismicity. Details of the regional seismicity can be obtained from the SCSN catalog via the Internet from the USGS Pasadena office or from Caltech (*www.trinet.org/scsn/scsn.html*).

Accelerometer Instrumentation

At the GVDA site, ground motion is measured in both a downhole array and a surface array. Figure 2 is a cross section showing the depth location of the borehole accelerometers, and Figure 3 is a map view showing the layout of the test site. Acceleration data are recorded at a rate of 500 samples per sec on a permanent 16-bit, 96-channel data acquisition system located in a trailer at the site. The borehole ground-motion sensors are dual-gain Kinemetrics FBA-23DH accelerometers capable of recording accelerations from $10^{-5}g$ to $2.0g$. These borehole accelerometers are located at depths of GL-6, GL-15, GL-22, GL-50, GL-220, GL-500, and GL-501 m below the surface (Fig. 2). A deep bedrock borehole that contains the GL-500- and GL-501-m accelerometers

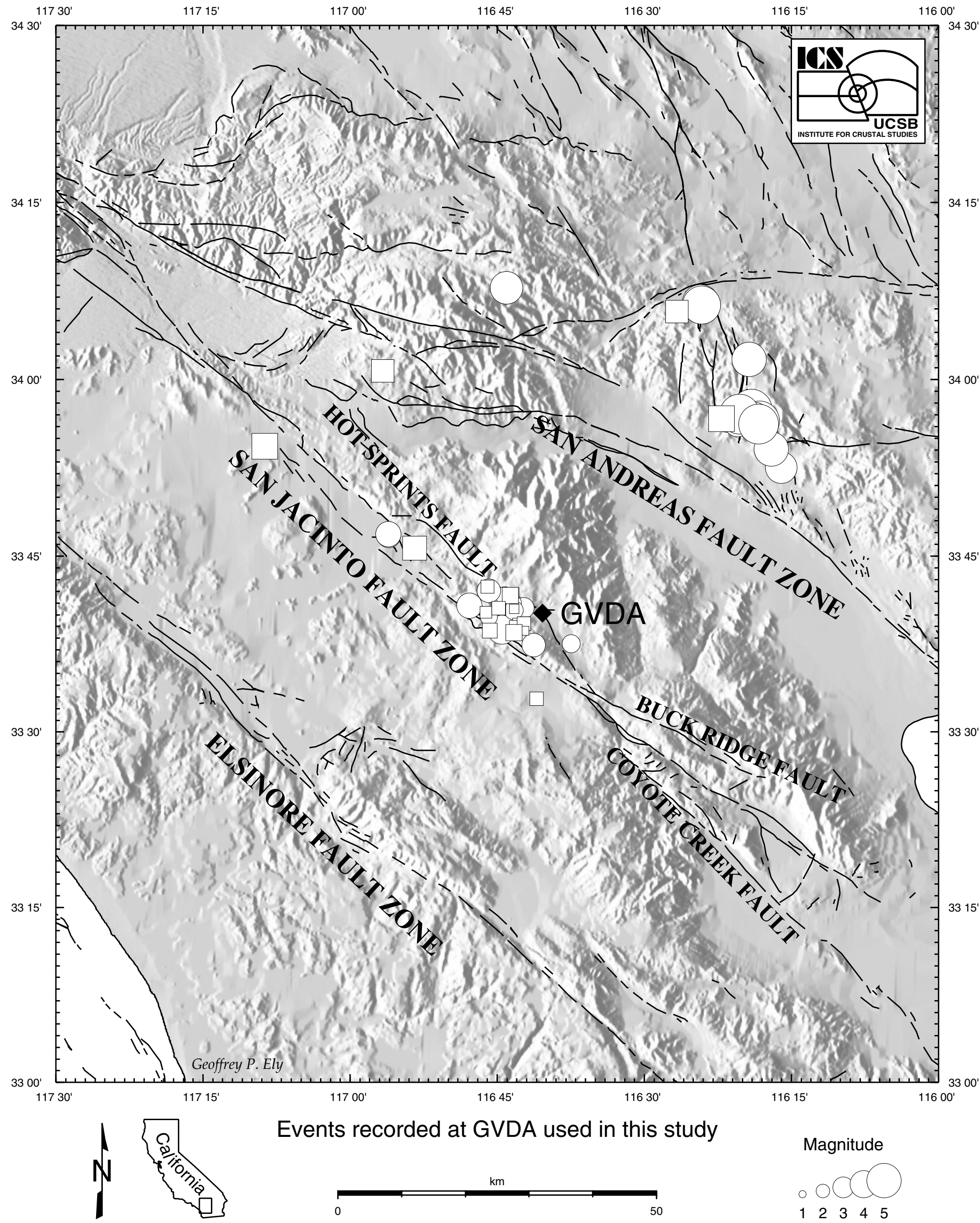

Figure 1. Regional map showing the 1992–1994 epicenters (circles) and 1995–1996 epicenters (squares) used in this study. The GVDA recording site is shown with a solid diamond. Shaded topography and faults (thin lines) are also shown.

is new (May 1995 installation) and not discussed in previous description of GVDA (Archuleta *et al.*, 1992).

A five-station array of sensors at the surface consists of Kinemetrics dual-gain FBA-23 accelerometers. Three of these extend linearly to the southeast of the borehole sensors at 61-m intervals, one directly above the borehole sensors and one 61 m to the northwest of the borehole sensors (Fig. 3). The final main station configuration has five surface accelerometers in a linear array spanning 244 m and five downhole accelerometers at depths from 6 to 501 m.

In addition to the main station at GVDA, a remote rock station was drilled and instrumented in 1998. A 30-m bedrock borehole contains another Kinemetrics FBA-23DH and is connected to a Kinemetrics 6-channel K2 recorder at the surface, where another FBA-23 is mounted to surface bedrock outcrop. The remote rock station is located about 3 km east of the main station.

Geotechnical Soil Properties

The material velocity at the GVDA site comes from three sources: (1) velocity logs by the USGS (Gibbs, 1989); (2) analysis of an 18-m core sample (Pecker and Moham-

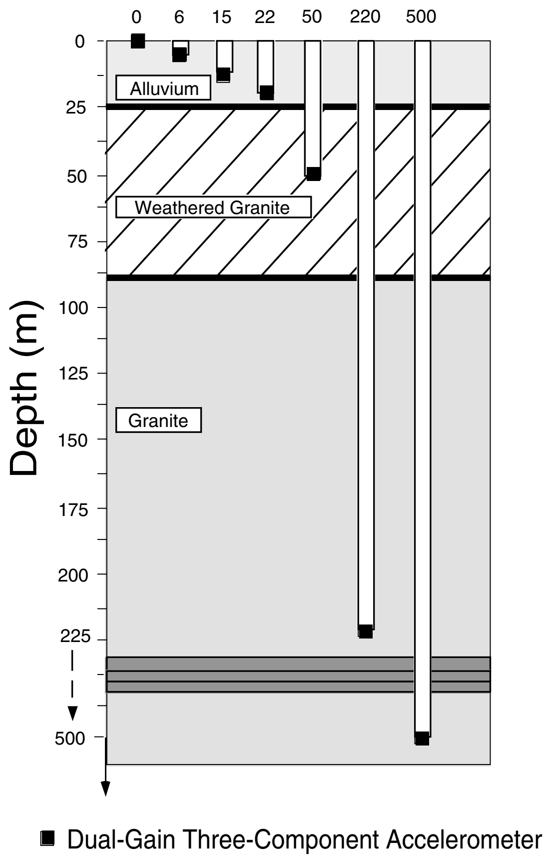

Figure 2. Cross section showing the depth of accelerometers at GVDA.

madioum, 1993); and (3) borehole suspension logging by Agbabian Associates of a 50-m borehole in November 1994 and a 100-m borehole in January 1996. The upper 25 m at the GVDA site consists of soil rich in organics and alluvium with average shear-wave velocities of 220 m/sec and compressional-wave velocities of 400 m/sec before the water table is reached at 1.5-m depth and above 1200 m/sec from the water table downward. Below 25 m a large zone of decomposed and weathered granite exists with shear-wave velocities ranging from 400 to 800 m/sec and compressional-wave velocities from 1700 to 2400 m/sec. Bedrock velocities determined from a depth below the weathered granite/granite interface in a 500-m borehole give values of 3150 m/sec for the shear wave and 5850 m/sec for the compressional wave using a 15-kHz signal for ultrasonic measurements. The interface between the competent bedrock with these high velocities and the weathered and decomposed granite occurs in the depth range of 87 to 95 m and may be a gradual change and not a distinct boundary. In addition, *P*- and *S*-wave velocities were also reported by Agbabian Associates (personal comm., 1995) from data collected in November 1994 and January 1996 for the upper 94 m at GVDA (Nigbor and Stellar, personal comm., 1996).

P- and *S*-wave velocities of the surface bedrock outcrop at the remote rock site 30-m borehole were measured with suspension logging in July 1998. *S*-wave velocity increases from 700 to 1400 m/sec in the top 4-m weathered zone. At 10–15 m it increases to 1700 m/sec, and below 15 m the *S*-wave velocity has an average value of approximately 2500 m/sec. *P*-wave velocity ranges from 3200 m/sec at the surface to 5000 m/sec at 30 m.

In addition to the measured shear-wave velocities (downhole and suspension), other geophysical and geotechnical methods have been used to characterize the GVDA site: gamma logs; guard and point resistivity; short and long normal resistivity; split spoon samples to 30 m; SPT measurements to 30 m; cone tip force, resistivity, and sleeve friction; dynamic pore pressure and seismic cone; soil classification; moisture content; dry density; and dynamic testing of Pitcher and Shelby samples.

Results from the dynamic testing of undisturbed soil specimens at GVDA from samples at GL-3.5-, GL-6.5-, GL-27.0-, and GL-41.3-m depth are presented by Stokoe and Darendeli (1998). The soil type corresponds to a nonplastic silty sand (SM, SUCS soil classification) for all samples. Cyclic behavior of the samples is typical of sands (Seed et al., 1986) with the shallower samples showing greater shear modulus degradation and larger damping with increased strain as compared to deeper samples.

Detailed Velocity Model of GVDA

Time Domain Modeling

In order to derive a detailed velocity model between the surface and GL-500-m depth, synthetic accelerograms were computed and compared with observations at different depths. A low-magnitude, impulsive earthquake was selected from the GVDA database for this comparison. The selected event has a local magnitude of *M* 3.2 and is located at 10 km from the site at a depth of 14.6 km. The focal characteristics of the earthquake are given in Table 1. Using the velocity models proposed by Gibbs (1989), Pecker and Mohammadioum (1993), and the velocity logs made by Agbabian and Associates (personal comm., 1995), synthetic accelerograms were computed at different depths and compared with observations. Synthetics were computed using the discrete wavenumber technique (Bouchon, 1981) in the frequency range from 0 to 10 Hz. The source was represented by a double couple with a 0.1-sec source time function.

Starting from a combination of the velocity models discussed previously, a trial-and-error procedure was applied. The *P*- and *S*-wave velocities, *Q* factors, and thicknesses were adjusted in order to obtain the best fit in both time and amplitude between the synthetics and the data. Table 2 gives the best final velocity model. Figure 4 compares observations (dark lines) and synthetics (light lines) at different depths of this model for the three components of ground acceleration. Note the good agreement between the observed and modeled time histories both in amplitude and arrival time of the body waves. The north–south component of the

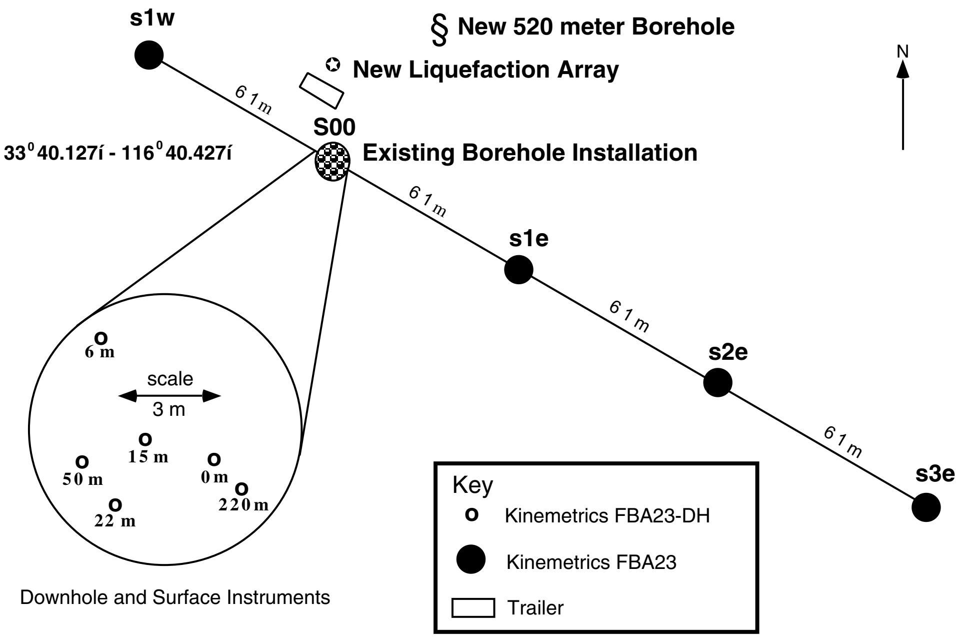

Figure 3. Map view of the GVDA test site showing the relative location of the surface stations, liquefaction array, boreholes, and main trailer.

Table 1
Focal Parameters of the Event Used to Calibrate the Velocity Model at GVDA

Date (yymmdd)	Time (hh:mm:ss)	M_L	Latitude	Longitude	Depth (km)	Strike	Dip	Rake	Event ID
95/12/26	05:44:11.00	3.2	33.7032	−116.7672	14.69	330°	50°	173°	9536005

Table 2
Velocity Model for the Garner Valley Downhole Array

Depth (m)	α (m/sec)	β (m/sec)	ρ (kg/m^3)	Q_P	Q_S
0–6	1225	175	2000	15	10
6–15	1525	200	2000	15	10
15–22	1600	320	2200	15	10
22–58	2000	550	2400	20	15
58–87	2150	650	2800	20	15
87–219	2820	1632	2800	50	30
219–600	5190	3000	2800	100	50
600–5000	5250	3050	2800	1000	500
>5000	6220	3490	2800	1000	500

GL-22 instrument did not work at the time of the event, but the corresponding synthetic is shown for completeness.

At GL-500 m, a good agreement is observed in the three components for both *P* and *S* waves indicating that the crustal velocity model is correct. Small amplitude late phases, corresponding to downgoing waves reflected at the free surface and velocity interfaces, are also correctly modeled. Similar observations can also be seen for GL-220 m, with the exception of the *S* wave on the vertical component, which is not correctly reproduced by the synthetics. At GL-50 m, similarly, both arrival times and amplitudes match between the data and the synthetics. From this depth to the surface, the major arrivals are matched by the synthetics; however, one can notice on the three components that late arrivals (after the *S* waves) are not reproduced by the synthetics. These arrivals may correspond to surface waves related to the two- or three-dimensional geometry of the 87-m interface. More detailed geotechnical investigations would be necessary to model these waves.

Another important effect is shear-wave anisotropy. Figure 5 shows the *S*-wave window of the observed (solid) and computed (dashed) north–south and east–west components at GL-0-m and GL-15-m depth. The synthetic *S*-wave arrival is late on both instruments in the north–south components. Because synthetics are calculated using an isotropic velocity model, these delays suggest anisotropic wave propagation in the soil at GVDA. Systematic rotation of horizontal components shows that this anisotropy is characterized by a fast axis along the north–south direction and a slow axis along the east–west direction. This result is in agreement with those previously obtained by Coutant (1996) and Kelner *et al.* (1999). In particular, Kelner *et al.* (1999) explained the shear-wave anisotropy at GVDA based on the presence of fractures in the granite. In addition, fracture analysis between 100- and 500-m depth at GVDA (Morin, 1995) shows the presence of a family of fractures predominantly oriented to the north.

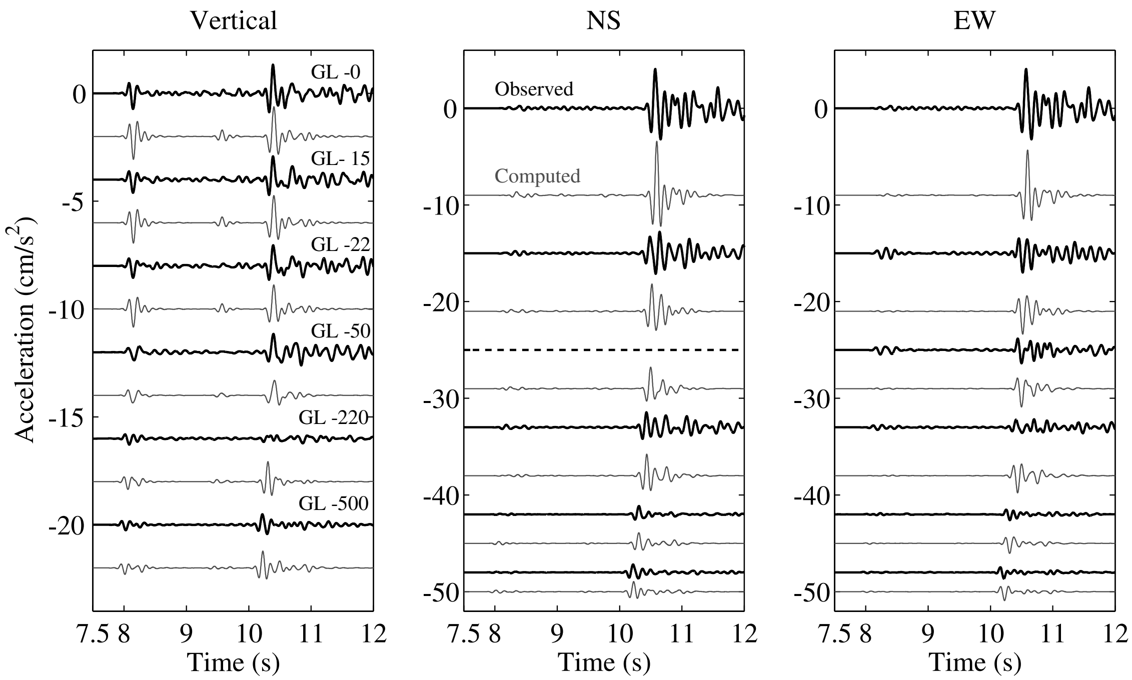

Figure 4. Time history modeling for event 9536005. The data are represented by the dark lines, and synthetics are represented by the light lines. North component for the GL-22 instrument was not working at the time of the event (dashed line).

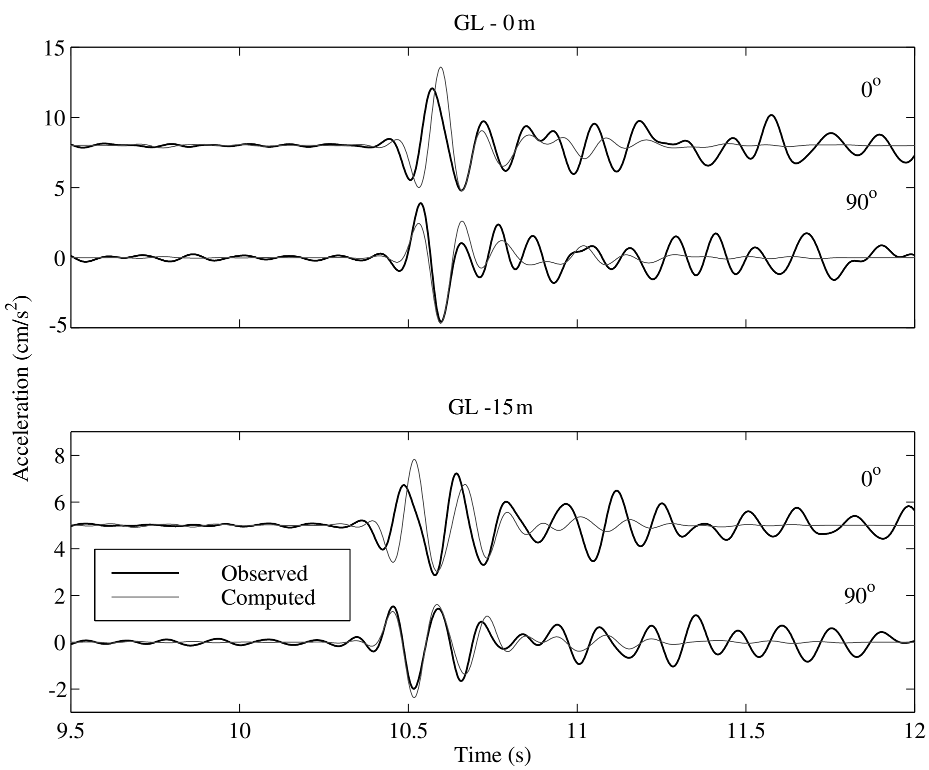

Figure 5. Shear-wave anisotropy observed at stations GL-0 and GL-15 on the north component for the *S*-wave window. The synthetic arrivals for the *S*-wave are delayed compared to the data.

Figure 6 shows synthetic acceleration time histories every 5 m from GL-150 m to the surface. Top traces represent the wavefield on the radial component, and bottom traces represent the wave field on the vertical component. The thickness of each stratum is depicted by the dashed lines. First, for the 1D velocity model, the wave propagation is not very complex, with reflections from the free surface and the velocity interfaces fading rapidly after the body waves have passed. Second, most of the energy is trapped between the surface and the GL-87 m boundary shown by the multiple reflections in Figure 6. Most of the amplification occurs in the first 6 to 15 m as shown by the strong amplitudes in the wave field for both the *P* and *S* waves. Third, the vertical component at the GL-87-m boundary shows that there are some waves arriving earlier than the direct *S* wave. These waves are *S* to *P* conversions that begin at that interface. Their effect is stronger at shallower depths. This is also observed in the data, in which the second strong arrival on the vertical components at GL-22, GL-15, and GL-0 m comes earlier than the direct *S*-waves on the horizontal components. Another converted wave can be observed on the horizontal component where a *P* to *S* conversion appears after the direct *P* arrival. This converted wave, also generated at the GL-87 m interface, is observed in the data, however with larger amplitude than that of the synthetics. This may be due to dipping layers at GVDA.

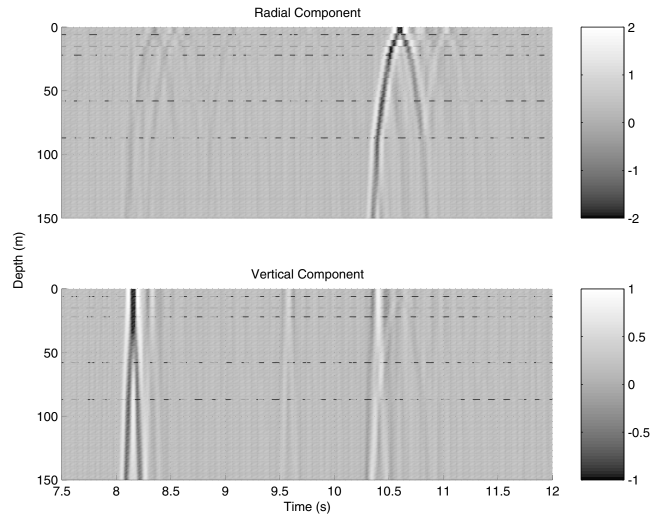

Figure 6. Synthetic acceleration time histories at GVDA. Top traces are the radial component, and bottom traces are the vertical component. The strata boundaries are in dashed lines. Note that at the GL-87-m boundary, on the vertical component, significant *S*-to-*P* conversions are observed. Conversely, from 58 m to the surface, on the radial component, *P*-to-*S* conversions are also present.

Observed and Theoretical Transfer Functions

In this article a subset of 54 events from the Landers and Joshua Tree aftershocks and from local earthquakes were analyzed. Figure 1 shows the location of the events as well as the stations used. Table 3 lists the hypocentral parameters of the events. These aftershocks have magnitudes from 1.3 to 6.1 and focal depths between 0.2 and 19.0 km. The instrument at GL-500 m was installed in May of 1995. Thus 28 events, mainly the Landers and Joshua Tree aftershocks, were used to compute the transfer functions from GL-0 to GL-220 m. The remaining 26 events, mainly local earthquakes since 1995 to 1996, were used to compute the transfer function between GL-0 to GL-500 m.

The transfer functions are evaluated using traditional spectral ratios of the *S* wave. A 10-sec window beginning 0.5 sec before the onset of the *S* wave is taken from each record. The noise level is taken from a 1-sec window of the *P* coda. A 5% Hanning taper was applied to all time windows. The spectra of the noise and the actual data were smoothed and reinterpolated to a common frequency interval, and only data with signal-to-noise ratio greater than 3 were used to compute the spectral ratios. The smoothing was done using a rectangle function 0.5 Hz wide. Once the spectral ratio for each station and each earthquake was obtained, the logarithmic average and the 95% confidence limits of the mean were calculated. Stations GL-6, GL-15, GL-22, GL-50, and GL-220 were used as reference sites for the events between 1992 and 1994, and station GL-500 was used for the events between 1995 and 1996.

Figure 7 shows empirical transfer functions (95% confidence region is shown by the shaded area) from the surface to the different depths were the sensors are located. Also shown are the outcrop and borehole response (solid and dashed lines) computed by the Haskell–Thompson propagator matrix method using the velocity profile obtained in the previous section. *Q* is assumed frequency indepent for this study. Recall that outcrop and borehole responses are defined in this article as the transfer functions computed when the motion of the reference site is the incident and total wave field, respectively. Notice the strong effect of the downgoing waves from the surface to 50-m depth, where the computed borehole responses match the empirical transfer functions. At GL-220 m and GL-500 m, this effect is reduced, where the outcrop responses match the empirical transfer functions. The latter is probably due to the attenuation in the upper layers that tapers off the reflections from the free surface and the velocity interfaces at those depths. In general, the velocity model allows one to reproduce the observed transfer functions reasonably well up to 20 Hz.

The Downgoing Wave Effect

For practical purposes it is desirable to have the transfer functions without downgoing wave effects so that the amplification factors and their resonant frequencies correspond to the actual values rather to pseudoresonances. In addition, another important application, when the incident wave field data are available, is to propagate downhole records to the surface through nonlinear soils, with elastic boundary con-

Table 3
Focal Parameters of the Earthquakes Used in This Study

Date (yymmdd)	Time (hh:mm:ss)	M_L	Lat.	Long.	Depth (km)	Event ID
89/12/02	23:16:45.23	4.2	33.6457	− 116.7420	14.47	8933623
89/12/22	03:03:22.84	3.4	33.6240	− 116.6880	14.08	8935603
90/10/16	13:01:22.34	2.6	33.6938	− 116.7370	18.00	9028913
91/05/20	15:04:9.864	3.5	33.7790	− 116.9340	12.39	9114015
91/05/20	15:00:53.11	3.7	33.7813	− 116.9350	12.77	9114015
92/03/13	07:47:12.91	2.7	33.8000	− 116.7800	15.74	9207307
92/04/23	02:25:32.51	4.6	33.9570	− 116.3170	11.93	9211402
92/04/23	04:50:25.51	6.1	33.9570	− 116.3170	12.38	9211404
92/04/26	09:55:47.68	3.6	33.9430	− 116.3590	6.61	9211709
92/05/04	01:16:4.953	4.1	33.9395	− 116.3410	5.97	9212501
92/05/04	16:19:52.45	4.9	33.9420	− 116.3040	12.54	9212516
92/05/06	02:38:45.95	4.7	33.9430	− 116.3150	7.31	9212702
92/05/18	15:44:20.43	4.9	33.9513	− 116.3380	7.10	9213915
92/06/29	16:01:42.63	4.7	33.8757	− 116.2670	1.86	9218116
92/06/29	14:13:39.63	5.4	34.1082	− 116.4040	9.88	9218114
92/06/29	14:08:38.63	5.6	34.1055	− 116.4020	11.20	9218114
92/06/30	21:22:54.88	4.8	34.1303	− 116.7340	12.47	9218221
92/07/05	04:18:40.13	3.1	33.6765	− 116.7040	17.83	9218704
92/07/24	18:14:35.59	5.0	33.9018	− 116.2840	9.08	9220618
92/07/25	04:31:59.59	4.9	33.9372	− 116.3050	5.85	9220704
93/04/25	16:30:22.40	2.3	33.6440	− 116.7170	12.32	9311516
93/05/12	05:49:13.90	2.6	33.6258	− 116.6240	3.74	9313205
93/08/21	01:46:39.25	5.1	34.0293	− 116.3210	9.05	9323301
93/09/22	22:35:54.75	2.4	33.6835	− 116.7230	15.01	9326522
94/04/22	02:33:2.634	2.5	33.6640	− 116.7640	13.29	9411202
94/10/11	23:14:36.74	2.8	33.6735	− 116.7210	14.85	9428423
94/11/07	18:32:15.52	3.8	33.7010	− 116.7640	14.98	9431118
94/11/09	02:28:59.77	3.7	33.6797	− 116.7970	17.17	9431302
95/05/30	01:44:56.12	3.1	33.5002	− 116.8245	13.83	9515001
95/07/28	07:07:30.39	3.6	33.5412	− 116.6903	8.60	9520907
95/08/22	16:57:24.74	2.2	33.6800	− 116.7255	13.50	9523416
95/11/29	02:51:06.15	2.2	33.6425	− 116.7250	12.52	9533302
95/12/24	19:16:23.59	2.6	33.5913	− 116.6360	10.13	9535819
95/12/26	05:44:11.00	3.2	33.7032	− 116.7672	14.69	9536005
96/01/04	02:34:33.09	1.4	33.6753	− 116.7210	14.06	9600402
96/01/05	11:57:40.14	3.8	33.9447	− 116.3685	6.94	9600511
96/01/13	03:59:23.08	2.0	33.5473	− 116.6833	6.00	9601303
96/01/17	08:56:05.08	1.8	33.6533	− 116.7132	13.73	9601708
96/01/20	08:11:34.95	1.7	33.6702	− 116.7695	13.01	9602008
96/01/21	12:01:18.40	3.3	34.0962	− 116.4448	8.20	9602112
96/01/23	23:02:38.41	2.1	33.6483	− 116.7170	11.86	9602323
96/01/25	16:00:53.75	1.8	33.6758	− 116.7458	16.38	9602516
96/01/25	20:47:03.31	1.7	33.6550	− 116.7047	15.40	9602520
96/01/27	05:47:26.23	1.9	33.7065	− 116.7670	14.11	9602705
96/01/27	06:25:10.02	1.5	33.6975	− 116.7225	14.29	9602706
96/03/16	03:29:24.09	2.0	33.6542	− 116.7043	13.93	9607603
96/04/11	04:43:25.37	2.4	33.6942	− 116.7278	15.33	9610204
96/08/23	03:24:02.37	1.3	33.6438	− 116.7040	17.01	9623603
96/09/12	21:18:18.32	3.8	33.9055	− 117.1452	14.05	9625621
96/10/09	21:06:02.16	2.2	33.6440	− 116.7625	8.11	9628321
96/10/17	11:46:35.50	2.0	33.6757	− 116.7477	10.57	9629111
96/11/25	04:43:08.37	3.3	34.0125	− 116.9445	14.16	9633004
96/12/02	03:47:22.55	2.4	33.6413	− 116.7217	10.60	9633703
96/12/28	22:41:20.23	3.5	33.7608	− 116.8907	13.14	9636322

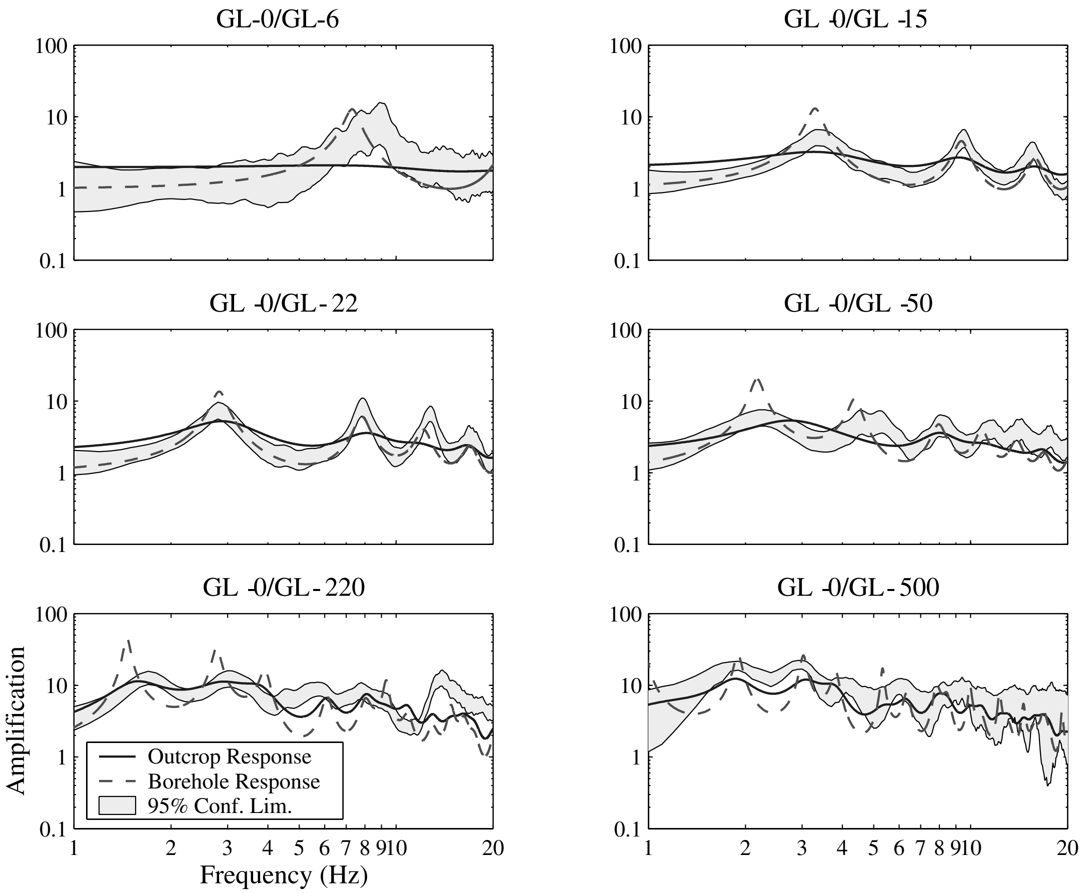

Figure 7. Empirical (shaded area), outcrop (solid), and borehole (dashed) responses between the surface and the different instruments at depth taken as reference sites. The shaded area represents the direct spectral ratio of the *S*-wave window and the 95% confidence limits of the mean.

ditions at the soil–bedrock interface (e.g. Joyner and Chen, 1975; Heuze *et al.*, 1997; Archuleta *et al.*, 1999)

Figure 7 shows the effect of the downgoing wave down to GL-50 m where the empirical transfer functions match the borehole response. At GL-220 m and GL-500 m, however, the empirical data match the outcrop response. This result suggests that in order to have the correct site response using borehole data, the instruments have to be deep enough to avoid the downgoing wave effect.

The results shown in Figure 7, obtained by taking the spectral ratio between the spectra of the surface and downhole records, imply the following relation:

$$\mathrm{Br}(\omega) = \frac{O(\omega)_{z=0}}{O^{\mathrm{T}}(\omega)_{z=H}}$$

where $O(\omega)_{z=0}$ is the observed spectrum of the ground motion at the surface, $O^{\mathrm{T}}(\omega)_{z=H}$ is the observed spectrum of the total ground motion at depth H, and $\mathrm{Br}(\omega)$ is the borehole response of the soil column, that is the response including the downgoing waves.

The fact that the empirical response matches the outcrop response at GL-220 and GL-500 m also implies

$$\mathrm{Or}(\omega) = \frac{O(\omega)_{z=0}}{2O^{\mathrm{I}}(\omega)_{z=H}}$$

where $O^{\mathrm{I}}(\omega)_{z=H}$ is the spectrum of the incident wave field at depth H and $\mathrm{Or}(\omega)$ is the outcrop response, that is, the response of the soil column excluding the downgoing waves. The factor of 2 takes into account the free-surface effect. This formulation is commonly used in the engineering practice to obtain the incident wave field from outcrop records (Schnabel *et al.*, 1972).

Thus, the incident motion can be factored from the previous equation above as

$$O^{\mathrm{I}}(\omega)_{z=H} = O^{\mathrm{T}}(\omega)_{z=H} \frac{\mathrm{Br}(\omega)}{2\mathrm{Or}(\omega)}$$

Both the outcrop and borehole responses can easily be computed provided that the velocity profile is known. This is our case as a result of the previous section, using the Haskell–Thompson method, for instance.

Figure 8 shows the computed incident wave field for the GL-50 sensor of the event listed in Table 1 using the procedure explained previously. The top trace is the computed downgoing wave field, the middle trace corresponds to the computed incident wave field, and the bottom trace is the observed total ground motion at GL-50 m on the east component. The synthetic computation shows the effect of the downgoing wave with two peaks at approximately 10.55 and 10.7 sec (top and bottom traces). These peaks are also observed in the recorded total motion at GVDA. In addition, Figure 9 shows the computed incident wave field at GL-50 m by deconvolving the outcrop response from the surface records (solid lines) and by the suggested method (dashed lines) for synthetic and observed data. As expected, the two methods give similar results. Although the *S* wave, as shown in the time history computations, cannot be modeled completely, most likely due to complications of the geometry of the site and basin effects, the direct *S* wave is well separated from the reflections coming from the free surface and from the interfaces at GVDA.

On the Applicability of the H/V Method to Estimate Site Response

Recently the H/V spectral ratio of the *S*-wave window has been used extensively for estimating site response. This method was introduced by Lermo and Chávez-García (1993) following the work done by Langston (1979), who studied the upper mantle and the crust from teleseismic records assuming that the vertical component is transparent to the site response. Because the site effect can be computed from a single station without the need of a nearby reference site, this method is quite inexpensive. Much of the work has been done trying to compare the H/V spectral ratio estimates with more traditional methods such as spectral ratios or generalized inversions of the *S*-wave spectra of the horizontal components only. These comparative studies (e.g., Lachet and Bard, 1994; Lachet *et al.*, 1996; Field and Jacob, 1995; Field, 1996; Theodulidis *et al.*, 1996; Bonilla *et al.*, 1997; Dimitriu *et al.*, 1998; Satoh *et al.*, 2001b; Tsuboi *et al.*, 2001) show that estimates of the frequency of the predominant peak are similar to those obtained with traditional spectral ratios; however, the absolute level of the site amplification does not correlate with the amplification obtained from those traditional methods.

Theodulidis *et al.* (1996) studied GVDA, and they compared the H/V spectral ratio on the surface with the surface-to-depth standard spectral ratio. They also compared with theoretical *S*-wave transfer functions derived from the vertical geotechnical profile, as well as with the H/V spectral ratio of synthetic seismograms generated by the discrete wavenumber method (Bouchon, 1981). Both theoretical and experimental data show a good stability of the H/V spectral ratio shape, which is in good agreement with the local structure; however, the absolute level of the H/V spectral ratio is different from the surface to depth spectral ratio.

One possibility for the difference between these methods is that the hypothesis by which the vertical component is transparent to the ground motion is not valid, and therefore the H/V spectral ratios produce different site response estimates compared to the traditional methods. This issue was recently addressed in the article by Tsuboi *et al.* (2001). In

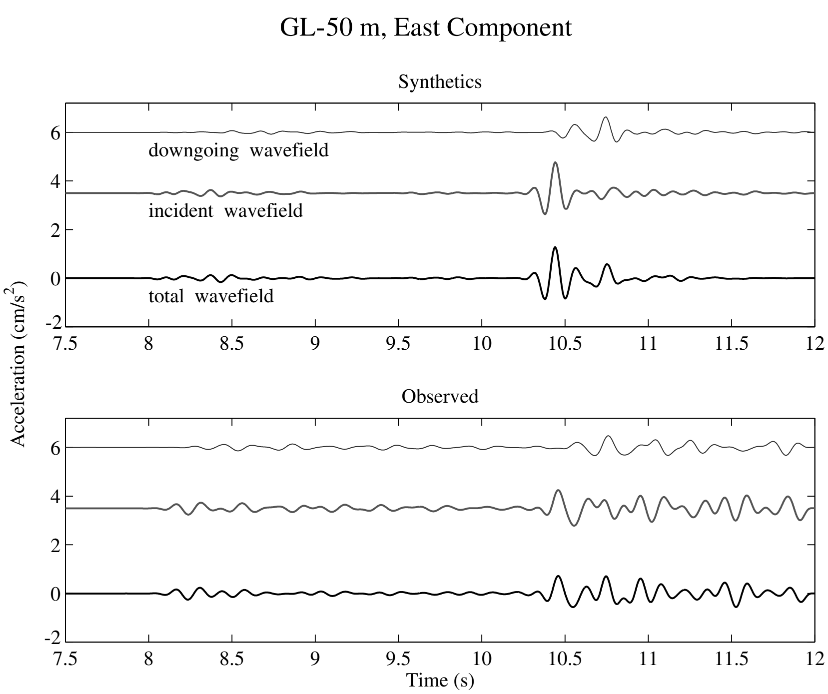

Figure 8. Incident wave field computation for the east component of event 9536005. Top subplot shows the technique on synthetics, and the bottom subplot shows the application on the data. In both subplots, the top trace is the computed downgoing wave field, the middle trace is the computed incident wave field, and the bottom trace is the observed total motion at GL-50 m.

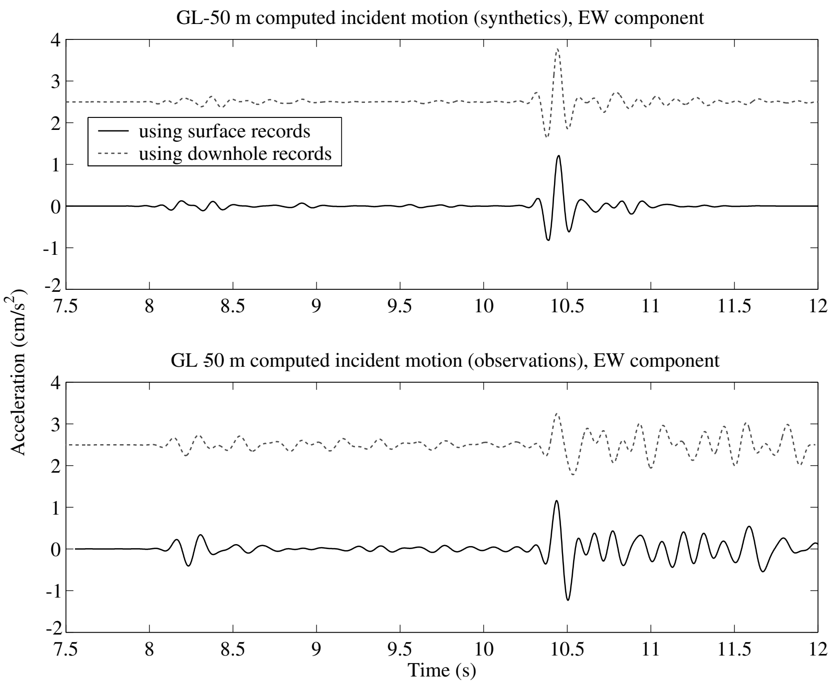

Figure 9. Computed incident wave field at GL-50 m for the east component of event 9536005. The solid line is the incident motion computed by deconvolving the outcrop response from the surface records. The dashed line is the incident motion computed by the proposed method in this article from the downhole records.

this section the H/V and the direct *S*-wave spectral ratio methods are compared using data recorded at GVDA.

Data and Methods

The same subset of 54 events used in the subsection about the transfer functions was used in this study. The methods used are the direct spectral ratio on the *S* wave and the H/V spectral ratio (Lermo and Chávez-García, 1993), respectively. The results from the direct spectral ratio on the *S* wave were already presented in the previous section about the computation of empirical transfer functions at GVDA. The H/V ratio or receiver-function estimate was introduced by Langston (1979) as a method to study the upper mantle and the crust from teleseismic records. The basic assumption in this technique is that the vertical component is not influenced by the local structure, whereas the horizontal components contain the *P* to *S* conversions due to the geology underlying the station. By deconvolving the vertical component from the horizontals, the site response is obtained.

Results

Theodulidis *et al.* (1996) studied the H/V spectral ratio at different depths in order to study the stability of the method to predict the resonant peaks. They, however, did not discuss the differences in amplitude compared to other more traditional techniques. They, however, already noted that the amplitude of the H/V spectral ratio is close to 1 as the sensor depth approaches to the bedrock. Figure 10 shows the average amplification factors from the direct spectral ratios on the *S* wave (thick line) and from the H/V spectral ratio (shaded area). The shaded areas represent the 95% confidence limits. Transfer functions from the surface down to 50-m depth were calculated using station GL-220 as reference site (1992–1994 data, circles in Fig. 1). Conversely, the transfer function at GL-220 m used station at GL-500 m as reference site (1995–1996 data, squares in Figure 1), and it is shown by the thick line. The H/V spectral ratios for the GL-220 and GL-500 stations are the light and dark shaded areas, respectively. Notice that, while the shape of the site response curves is similar (H/V is stable to obtain the resonant peaks), there is a discrepancy in the absolute level of amplification, similar to what has been shown by previous studies (e.g., Theodulidis *et al.*, 1996). This result suggests that the vertical component has its own site response.

In order to investigate why the amplification obtained from the H/V spectral ratio is different from the one computed by the direct *S*-wave spectral ratio, the transfer functions of the *S* wave on the vertical components are shown in Figure 11 (shaded area). In addition, if the incoming waves are not exactly vertically incident, the *S*-wave window on the vertical component may contain significant *S*-to-*P* converted waves as seen on the wave propagation characteristics at GVDA (Fig. 6). Using the Haskell–Thompson method, synthetic borehole responses (solid lines) with the P-wave velocity were computed and superimposed on the direct *S*-wave spectral estimates in Fig. 11.

First, it is clearly seen that the vertical components have their own amplification around 5–10 between 3 and 4 Hz. Consequently, the fundamental assumption of the H/V method (vertical component free of site response) is invalidated. Also, notice the agreement between the empirical and computed transfer functions. The fact that the empirical site response matches the computed *P*-wave site response confirms the presence of *S*-to-*P* converted waves above the 87-m interface in the data. Conversely, at GL-220 m and GL-500

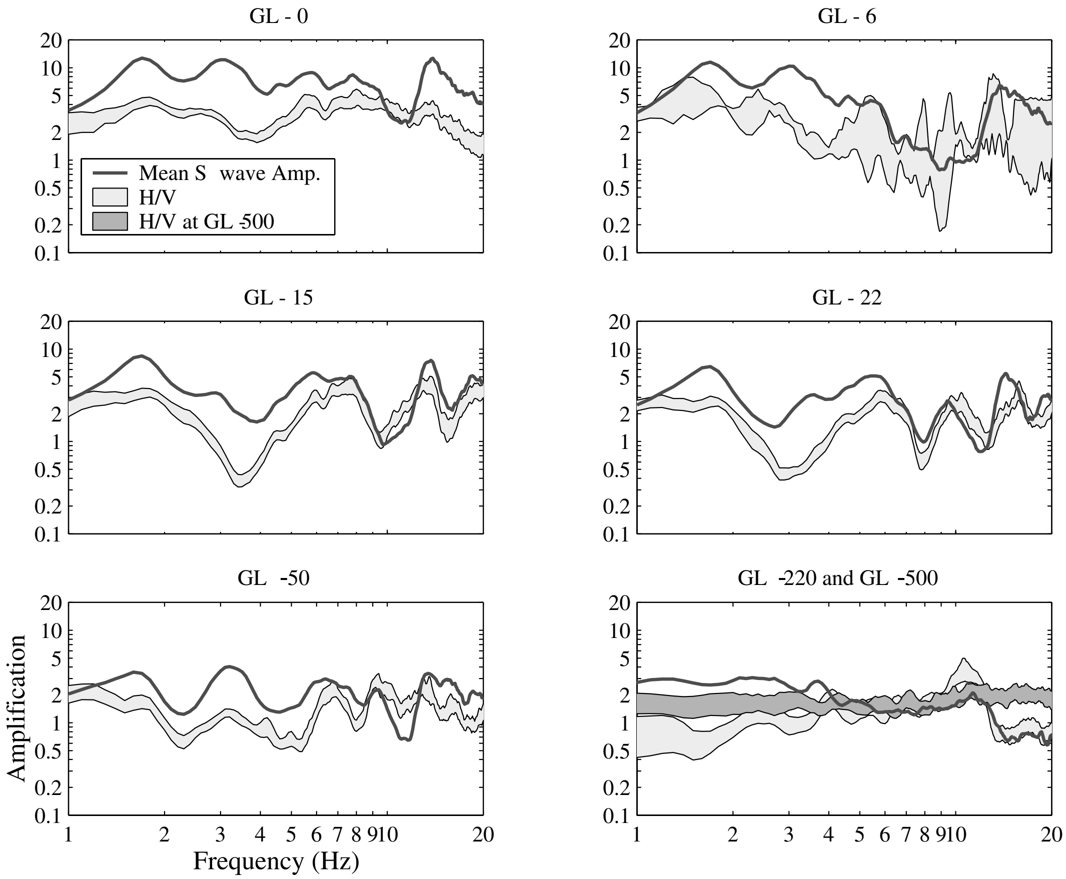

Figure 10. Site response obtained from the direct *S* wave (thick line) and H/V spectral ratios (shaded area). The shaded area represents the 95% confidence limits. Dark shaded area corresponds to the H/V spectral ratio for the GL-500 instrument.

m, the H/V spectral ratio is close to 1. These stations are in competent granite, and similarly to what was shown by Bonilla *et al.* (1997) and Dimitriu *et al.* (1998), the site response for rock sites calculated by direct *S*-wave and H/V spectral ratios is close to 1.

Finally, in order to test the effect of an oblique incident wave field, two *SV* GL-0/GL-500-m transfer functions with angles of incidence of 20° and 30° were computed and compared to the other estimates (Fig. 12). It is observed that the spectral amplification between 1 and 4 Hz is better modeled for an oblique wave field than a vertical one. However, for higher frequencies, this effect is opposite. One possibility is to consider frequency-dependent Q to compute the theoretical transfer functions (Satoh *et al.*, 1995). This subject will be considered in a further study of the GVDA through an inversion of its velocity structure. Conversely, the H/V spectral ratio correctly maps the location of the resonant peaks compared to the other methods.

In the GVDA case, the H/V spectral ratio, or receiver-function estimates, are capable of revealing the predominant frequency peaks; however, their amplification values are different from the amplifications determined from the *S* wave because the vertical components have their own site response produced by *S*-to-*P* conversions at the 87-m boundary.

Conclusions

The direct observation of ground motion in vertical arrays has provided fundamental data for the interpretation and analysis of the effects of near-surface geology on seismic ground motion. At the GVDA array the effects of amplification and attenuation are modeled using ground motion from small to moderate earthquakes. The observed surface ground motion is reproduced using the geotechnical site characterization data, the observed borehole motions, and a linear wave propagation technique due to the relatively low ground-motion amplitudes. Calibration of linear wave propagation techniques with low strain observations is important before moving into the nonlinear large-strain domain. The vertical array data allow one to directly study the effects of the near-surface soil conditions on ground motion and are critical to the development and validation of numerical techniques to correctly reproduce site response effects at all strain levels. Furthermore, with regard to the engineering characteristics of seismic input, the observations at the

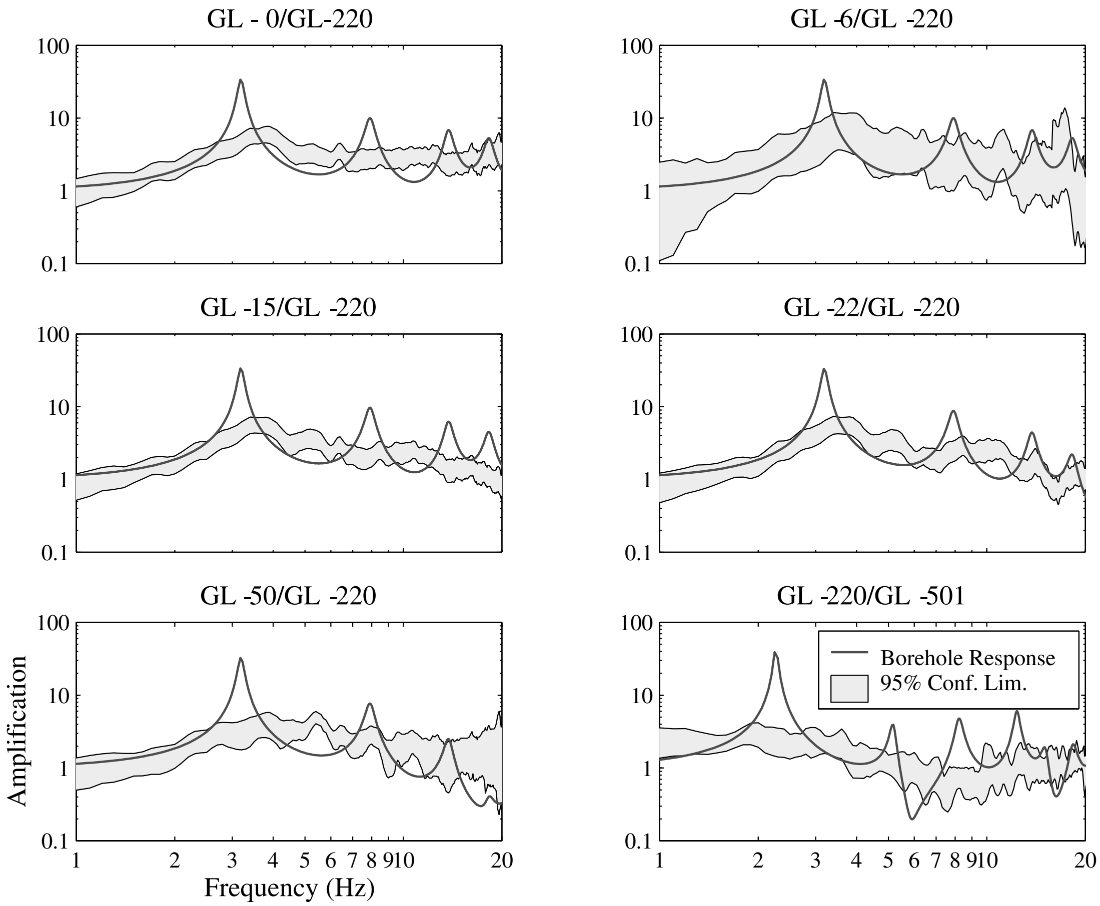

Figure 11. Site response obtained from the direct spectral ratio method of the *S* wave on the vertical components (shaded area). In addition, the borehole (solid) *P*-wave responses are also shown. Notice that the vertical components have their own amplification about 5–10 between 3.0 and 4.0 Hz. The match between synthetics and empirical transfer functions confirm the presence of significant *S*-to-*P* converted waves at the vertical component.

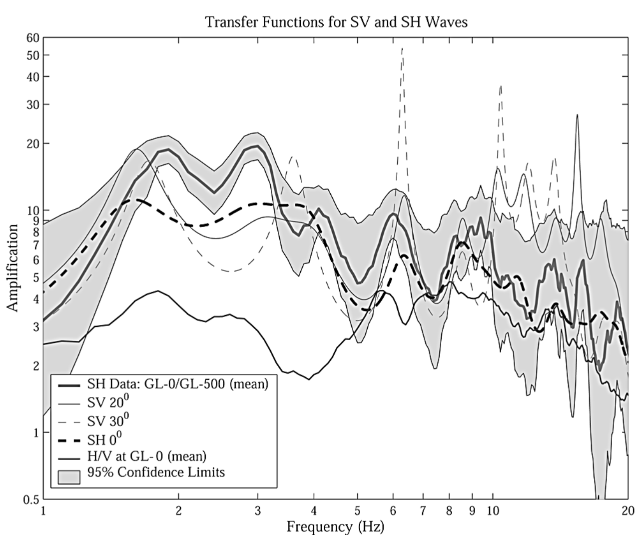

Figure 12. Comparison among oblique *SV*, vertically incident *SH*, H/V spectral ratios, and empirical GL-0/GL-500-m transfer functions.

GVDA vertical array helped to test a simple technique to compute the incident wave field at depth, which is needed for nonlinear site response analysis.

Wave propagation at GVDA is controlled by the strong impedance constrast at the 87-m boundary. Most of the energy is trapped between the surface and this depth. In addition, there are significant *S*-to-*P* converted waves on the vertical component, causing this component to have its own site response. The latter fails the H/V spectral ratio method because its fundamental assumption that the vertical component is transparent to the local site response is violated.

Although most of the wave propagation characteristics can be explained by a simple 1D model, there are important effects of the basin geometry that may affect the ground motion recorded at GVDA. Further studies are needed to reveal the basin effects at this engineering test site.

Acknowledgments

The authors wish to thank Robert Nigbor and Robert Stellar of Agbabian Associates, who have provided much assistance on the GVDA project. Thanks to Mr. Scott Swain of Institute for Crustal Studies, the GVDA project engineer, who keeps the project running. We are indebted to Leonard Hale, Robert Linquist, and the entire staff at the Lake Hemet Municipal Water District for their assistance and permission to use the land at GVDA. We would also like to thank Toshimi Satoh, Francois Heuze, David Oglesby, Stephane Nechtschein, and an anonymous reviewer for their invaluable comments. This work was supported by the U.S. Nuclear Regulatory Commission, NRC-04-96-046, and the French Institut de Protection et de Sureté Nucléaire (IPSN) No. 406000000470.

References

Abercrombie, R. E. (1997). Near-surface attenuation and site effects from comparison of surface and deep borehole recording, *Bull. Seism. Soc. Am.* **87,** 731–744.

Aguirre, J., and K. Irikura (1997). Nonlinearity, liquefaction, and velocity variation of soft soil layers in Port Island, Kobe, during the Hyogo-ken Nanbu earthquake, *Bull. Seism. Soc. Am.* **87,** 1244–1258.

Archuleta, R. J., L. F. Bonilla, and D. Lavallée (1999). Nonlinear site response using generalized Masing rules coupled with pore pressure, in *Proceedings of the OECD-NEA Workshop on the Engineering Characterization of Seismic Input*, Brookhaven National Laboratory, New York, Upton, 32 pp.

Archuleta, R. J., S. H. Seale, P. V. Sangas, L. M. Baker, and S. T. Swain (1992). Garner Valley downhole array of accelerometers: instrumentation and preliminary data analysis, *Bull. Seism. Soc. Am.* **82,** 1592–1621.

Archuleta, R. J., S. H. Seale, P. V. Sangas, L. M. Baker, and S. T. Swain (1993). Garner Valley downhole array of accelerometers: instrumentation and preliminary data analysis, *Bull. Seism. Soc. Am.* **83,** 2039.

Bonilla, L. F., J. H. Steidl, G. T. Lindley, A. G. Tumarkin, and R. J. Archuleta (1997). Site amplification in the San Fernando Valley, California: variability of site-effect estimation using the *S*-wave, coda, and H/V methods, *Bull. Seism. Soc. Am.* **87,** 710–730.

Boore, D. M., and W. B. Joyner (1997). Site amplification for generic rock sites, *Bull. Seism. Soc. Am.* **87,** 327–341.

Borcherdt, R. D. (1970). Effects of local geology on ground motion near San Francisco Bay, *Bull. Seism. Soc. Am.* **60,** 29–61.

Bouchon, M. (1981). A simple method to calculate Greens functions for elastic layered media, *Bull. Seism. Soc. Am.* **71,** 959–971.

Coutant, O. (1996). Observation of Shallow Anisotropy on Local Earthquake Records at the Garner Valley, Southern California, Downhole Array, *Bull. Seism. Soc. Am.* **86,** 477–488.

Dimitriu, P. P., Ch. A. Papaioannou, and N. P. Theodulidis (1998). EURO-SEISTEST strong-motion array near Thessaloniki, northern Greece: a study of site effects, *Bull. Seism. Soc. Am.* **88,** 862–873.

Field, E. H. (1996). Spectral amplification in a sediment-filled valley exhibiting clear basin-edge induced waves, *Bull. Seism. Soc. Am.* **86,** 991–1005.

Field, E. H., and K. H. Jacob (1995). A comparison and test of various site response estimation techniques, including three that are non reference-site dependent, *Bull. Seism. Soc. Am.* **85,** 1127–1143.

Gibbs, J. F. (1989). Near-surface P- and S-wave velocities from borehole measurements near Lake Hemet, California, *U.S. Geol. Surv. Open-File Rept. 89-630*.

Hartzell, S. H. (1992). Site response estimation from earthquake data, *Bull. Seism. Soc. Am.* **82,** 2308–2327.

Hartzell, S. H., A. Leeds, A. Frankel, and J. Michael (1996). Site response for urban Los Angeles using aftershocks of the Northridge earthquake, *Bull. Seism. Soc. Am.* **86,** S168–S192.

Heuze, F. E., T.-S. Ueng, L. J. Hutchings, S. P. Jarpe, and P. W. Kasameyer (1997). A coupled seismic-geotechnical approach to site-especific strong motion, *Soil Dyn. Earthquake Eng.* **16,** 259–272.

Iai, S., T. Morita, T. Kameoka, Y. Matsunaga, and K. Abiko (1995). Response of a dense sand deposit during 1993 Kushiro-Oki Earthquake, *Soils Foundations* **35,** 115–131.

Joyner, W., and A. T. Chen (1975). Calculation of Nonlinear Ground Response in Earthquakes, *Bull. Seism. Soc. Am.* **65,** 1315–1336.

Kato, K., K. Aki, and M. Takemura (1995). Site amplification from codawaves: validation and application to S-wave site response, *Bull. Seism. Soc. Am.* **85,** 467–477.

Kelner, S., M. Bouchon, and O. Coutant (1999). Characterization of fractures in shallow granite from the modeling of the anisotropy and attenuation of seismic waves, *Bull. Seism. Soc. Am.* **89,** 706–717.

Kinoshita, S. (1992). Local characteristic of the fmax of bedrock motion in the Tokyo metropolitan area, Japan, *J. Phys. Earth* **40,** 487–515.

Lachet, C., and P.-Y. Bard (1994). Numerical and theoretical investigations on the possibilities and limitations of Nakamura's technique, *J. Phys. Earth* **42,** 377–397.

Lachet, D., Hatzfeld, C., P.-Y. Bard, N. Theodulis, C. Papaioannou, and A. Savvaidis (1996). Site effects and microzonation in the city of Thessaloniki (Greece): comparison of different approaches, *Bull. Seism. Soc. Am.* **86,** 1692–1703.

Langston, C. A. (1979). Structure under Mount Rainier, Washington, inferred from teleseismic body waves, *J. Geophys. Res.* **84,** 4749–4762.

Lermo, J., and F. J. Chávez-García (1993). Site effect evaluation using spectral ratios with only one station, *Bull. Seism. Soc. Am.* **83,** 1574–1594.

Margheriti, L., L. Wennerberg, and J. Boatwright (1994). A comparison of coda and S-wave spectral ratio estimates of site response in the southern San Francisco Bay area, *Bull. Seism. Soc. Am.* **84,** 1815–1830.

Morin, R. (1995). Fracture analysis for the Garner Valley well, Institute for Crustal Studies, internal report.

Nagumo, H., and T. Sasatani (1998). The characteristics of observed waveforms on the small Kaminokuni basin, Hokkaido, Japan, in *The Effects of Surface Geology on Seismic Motion*, K. Irikura, K. Kudo, H. Okada, and T. Sasatani (Eds.), Balkema, Rotterdam, 503–508.

Pecker, A., and B. Mohammadioum (1993). Garner Valley: analyse statistique de 218 enregistrements seismiques, in *Proceedings of the 3eme Colloque National AFPS*, Saint-Remy-les-Chevreuse, France.

Rockwell, T., C. Loughman, and P. Merifield (1990). Late quaternary rate of slip along the San Jacinto fault zone near Anza, Southern California, *J. Geophys. Res.*, **95,** 8593–8605.

Sato, K., T. Kokusho, M. Matsumoto, and E. Yamada (1996). Nonlinear seismic response and soil property during strong motion, in *Special Issue of Soils and Foundations in Geotechnical Aspects of the January 17, 1995, Hyogoken-Nambu Earthquakes,* 41–52.

Satoh, T., H. Kawase, and T. Sato (1995). Evaluation of local site effects and their removal from borehole records observed in the Sendai region, Japan, *Bull. Seism. Soc. Am.* **85,** 1770–1789.

Satoh, T., M. Fushimi, and Y. Tatsumi (2001a). Inversion of strain-dependent nonlinear characteristics of soils using weak and strong motions observed by boreholes sites in Japan, *Bull. Seism. Soc. Am.* **91,** 365–380.

Satoh, T., H. Kawase, and S. Matsushima (2001b). Differences between site characteristics obtained from microtremors, S-waves, P-waves, and codas, *Bull. Seism. Soc. Am.* **91,** 313–334.

Schnabel, P., H. B. Seed, and J. Lysmer (1972). Modification of seismograph records for effects of local soil conditions, *Bull. Seism. Soc. Am.* **62,** 1649–1664.

Seed, H. B., and I. M. Idriss (1970). Analyses of Ground Motions at Union Bay, Seattle during earthquakes and distant nuclear blasts, *Bull. Seism. Soc. Am.* **60,** 125–136.

Seed, H. B., R. M. Wong, I. M. Idriss, and K. Tokimatsu (1986). Moduli of damping factors for dynamic analyses of cohesionless soils, *J. Soil Mech. Found. Div.* **112,** no. SM11, 1016–1032.

Sharp, R. V. (1967). San Jacinto fault zone in the Peninsular Ranges of southern California, *Geol. Soc. Am. Bull.* **78,** 705–730.

Steidl, J. H., A. G. Tumarkin, and R. J. Archuleta (1996). What is a reference site? *Bull. Seism. Soc. Am.* **86,** 1733–1748.

Stokoe, K. H., and M. B. Darendeli (1998). Laboratory evaluation of the dynamic properties of intact soil specimens, Garner Valley, California, Institute for Crustal Studies Internal Report, 32 pp.

Su, F., J. G. Anderson, J. N. Brune, and Y. Zeng (1996). A comparison of direct S-wave and coda wave site amplification determined from aftershocks of Little Skull Mountain earthquake, *Bull. Seism. Soc. Am.* **86,** 1006–1018.

Theodulidis, N., R. J. Archuleta, P.-Y. Bard, and M. Bouchon (1996). Horizontal to vertical spectral ratio and geological conditions: the case of Garner Valley downhole array in southern California, *Bull. Seism. Soc. Am.* **86,** 306–319.

Tsuboi, S., M. Saito, and Y. Ishihara (2001). Verification of horizontal-to-vertical spectral ratio technique for estimation of site response using borehole seismographs, *Bull. Seism. Soc. Am.* **91,** 499–510.

Wen, K., I. Beresnev, and Y. T. Yeh (1994). Nonlinear soil amplification inferred from down hole strong seismic motion data, *Geophys. Res. Lett.* **21,** 2625–2628.

Zeghal, M., and A. W. Elgamal (1994). Analysis of Site Liquefaction Using Earthquake Records, *J. Geotech. Eng.* **120,** no. 6, 996–1017.

Institute for Crustal Studies
University of California at Santa Barbara
Santa Barbara, California 93106-1100
(L.F.B., J.H.S., R.J.A.)

Department of Geological Sciences
University of California at Santa Barbara
Santa Barbara, California 93106-1100
(L.F.B., R.J.A.)

Institut de Radioprotection et de Sûreté Nucléaire
Fontenay-aux-Roses, CEDEX
France
(J.C.G., L.F.B.)

Manuscript received 27 August 2001.